Monthly Notices
of the
ROYAL ASTRONOMICAL SOCIETY

MNRAS **499,** 1795–1804 (2020)
Advance Access publication 2020 September 23

doi:10.1093/mnras/staa2903

Deuterium fractionation of nitrogen hydrides: detections of NHD and ND_2

A. Bacmann [1]★ A. Faure [1]★ P. Hily-Blant [1] K. Kobayashi,[2] H. Ozeki,[3] S. Yamamoto,[4] L. Pagani[5] and F. Lique[6]

[1]*Univ. Grenoble Alpes, CNRS, IPAG, 38000 Grenoble, France*
[2]*Department of Physics, University of Toyama, 3190 Gofuku, Toyama 930-8555, Japan*
[3]*Department of Environmental Science, Faculty of Science, Toho University, 2-2-1 Miyama, Funabashi, Chiba 274-8510, Japan*
[4]*Department of Physics, The University of Tokyo, 7-3-1, Hongo, Bunkyo-ku, Tokyo 113-0033, Japan*
[5]*LERMA & UMR8112 du CNRS, Observatoire de Paris, PSL University, Sorbonne Universitś, CNRS, F-75014 Paris, France*
[6]*LOMC – UMR 6294, CNRS, Université du Havre, 25 rue Philippe Lebon, BP 1123, F-76063 Le Havre Cedex, France*

Accepted 2020 September 11. Received 2020 September 11; in original form 2020 July 10

ABSTRACT

Although ammonia is an abundant molecule commonly observed towards the dense interstellar medium, it has not yet been established whether its main formation route is from gas-phase ion–molecule reactions or grain-surface hydrogen additions on adsorbed nitrogen atoms. Deuterium fractionation can be used as a tool to constrain formation mechanisms. High abundances of deuterated molecules are routinely observed in the dense interstellar medium, with the ratio between deuterated molecules and the main isotopologue enhanced by several orders of magnitude with respect to the elemental D/H ratio. In the case of ammonia, the detection of its triply deuterated isotopologue hints at high abundances of the deuterated intermediate nitrogen radicals, ND, NHD, and ND_2. So far however, only ND has been detected in the interstellar medium. In this paper, to constrain the formation of ammonia, we aim at determining the NHD/NH_2 and ND_2/NHD abundance ratios, and compare them with the predictions of both pure gas-phase and grain-surface chemical models. We searched for the fundamental rotational transitions of NHD and ND_2 towards the class 0 protostar IRAS16293−2422, towards which NH, NH_2 and ND had been previously detected. Both NHD and ND_2 are detected in absorption towards the source. The relative abundance ratios NH_2:NHD:ND_2 are close to 8:4:1. These ratios can be reproduced by our gas-phase chemical model within a factor of 2–3. Statistical ratios as expected from grain-surface chemistry are also consistent with our data. Further investigations of the ortho-to-para ratio in ND_2 , both theoretical and observational, could bring new constraints to better understand nitrogen hydride chemistry.

Key words: astrochemistry – stars: formation – stars: protostars – ISM: individual objects: IRAS16293-2422 – ISM: molecules.

1 INTRODUCTION

High degrees of deuterium fractionation in interstellar molecules have long been observed towards star-forming regions, in particular towards the cold and dense prestellar cores and envelopes of protostars. Indeed, because of the lower zero-point energy of H_2D^+ compared to that of H_3^+, the deuterium exchange reaction $H_3^+ + HD \rightarrow H_2 + H_2D^+$ is slightly exothermic and favoured at temperatures lower than 20 K, increasing the H_2D^+/H_3^+ ratio and therefore the possibility of transferring a deuterium atom to molecular species by ion-neutral chemistry. This ratio is further enhanced when CO, which is a major destroyer of the H_3^+ ions, is frozen out on dust grains and undergoes a drastic abundance drop. In this case, the above-mentioned reaction becomes the main reaction destroying H_3^+, which leads to an increased H_2D^+/H_3^+ ratio, reaching sometimes unity, according to some models (Pagani, Salez & Wannier 1992; Roberts, Herbst & Millar 2003). Similar reactions with all deuterated isotopologues of H_3^+ also take place, leading to high abundances of H_2D^+, D_2H^+, and D_3^+ (Roberts et al. 2003; Walmsley, Flower & Pineau des Forêts 2004).

Deuterium fractionation can theoretically be used to constrain molecular formation pathways, because the ratios between the deuterated species and the main isotopologue are expected to be different if the molecule forms in the gas-phase or as a result of grain-surface chemistry. In the latter case, deuteration is expected to follow a statistical scheme, as highlighted in, e.g. Brown & Millar (1989). The deuteration of such a ubiquitous molecule as ammonia has stimulated many studies, especially since the discovery of its triply deuterated isotopologue by Lis et al. (2002b) and van der Tak et al. (2002) with an abundance ratio $ND_3/NH_3 \sim 0.001$, an increase of 12 orders of magnitude with respect to the elemental D/H ratio (Linsky et al. 2006), challenging chemical models. As likely precursors of ammonia, nitrogen hydrides can bring valuable clues to constrain ammonia formation mechanisms. Roueff, Loison & Hickson (2015) argue that highly deuterated ammonia can form from pure gas-phase chemistry. Observations of deuterated nitrogen hydride radicals like NHD and ND_2 can help to test this type of scenario.

The *Herschel Space Observatory*[1] has allowed us to access the fundamental rotational transitions of nitrogen hydrides. Since its launch

★ E-mail: aurore.bacmann@univ-grenoble-alpes.fr (AB), alexandre.faure@univ-grenoble-alpes.fr (AF)

[1]*Herschel* is an ESA space observatory with science instruments provided by European-led Principal Investigator consortia and with important participation from NASA

in 2009, both the NH radical and its deuterated counterpart have been detected towards the low-mass class 0 protostar IRAS16293−2422 (Bacmann et al. 2010) and towards the dark core IRAS16293E (Bacmann et al. 2016). The abundances derived for these species have been found to be consistent with the model predictions of Roueff et al. (2005) and Roueff et al. (2015). The NH_2 radical has also been detected towards IRAS16293−2422 (Hily-Blant et al. 2010) but no detection of its singly isotopologue NHD or doubly deuterated isotopologue ND_2 had been reported until recently. However, while this manuscript was under revision, Melosso et al. (2020) presented the detection of the two latter species in IRAS16293−2422.

In this paper, we report the detection of both NHD and *para*-ND_2 towards IRAS16293−2422, based on different transitions from those in Melosso et al. (2020), and discuss the implications of the derived abundances and abundance ratios on the formation of nitrogen hydrides. The observations are presented in Section 2. In Section 3, we derive the abundances and discuss them in the light of new chemical models in Section 4, before concluding in Section 5.

2 OBSERVATIONS

The search for NHD and ND_2 was conducted towards IRAS16293−2422 which is a class 0 low-mass protostar where NH, ND, and NH_2 had already been discovered (Bacmann et al. 2010; Hily-Blant et al. 2010). The coordinates of integration for the observations are $\alpha_{2000} = 16^h32^m22.8^s$ $\delta_{2000} = -24°28'33''$, the same as those where the nitrogen hydrides were previously detected. While the source is a binary (composed of two sources A and B) (see Jørgensen et al. 2016, for an extensive description of the source), the separation between the components is 5.1 arcsec, so that our observations encompass both components. The species NH, ND, and NH_2 were all seen in absorption against a background emitted by the warm dust. This is partly due to the very high critical densities of the fundamental rotational transitions of nitrogen hydrides, especially NH_2 and NH (around 10^7 cm^{-3}, see Dumouchel et al. 2012; Bouhafs et al. 2019, for the derivation of the collisional rate coefficients), and the presence of the species in the lower density envelope. Indeed, the frequency of the fundamental rotational transition of ND is a factor of 2 smaller than for NH, and therefore the critical density a factor of ∼10 smaller, making ND easier to be seen in emission than its hydrogenated counterpart.

2.1 Spectroscopy

Microwave spectroscopy measurements and analysis of NHD have been performed by Kobayashi et al. (1997) and Motoki, Ozeki & Kobayashi (2013), while those for ND_2 have been performed by Kanada, Yamamoto & Saito (1991) and Melosso, Degli Esposti & Dore (2017). The spectra of both radicals have a complex fine and hyperfine structure due to the interaction with the electronic and nuclear spins of nitrogen, deuterium and hydrogen (the latter only for NHD). For NHD, we targeted the group of hyperfine components ($N_{K_aK_c}J$: 1_{01} 3/2–0_{00} 1/2) around 412.7 GHz. The $N_{K_aK_c}J$: 1_{01} 1/2–0_{00} 1/2 transition at 413.5 GHz was additionally present in our observing bandwidth. For ND_2, the transitions ($N_{K_aK_c}J$: 1_{11} 1/2–0_{00} 1/2) at 531 GHz were observed, which correspond to *para*-ND_2. The frequencies of the transitions and their Einstein coefficients for spontaneous emission are given in Tables A1 and A2 for NHD and in Table A3 for ND_2.

2.2 NHD observations

Singly deuterated amidogen was searched for with the APEX telescope[2] on Chajnantor Plateau, Chile. The observations (programme number E-091.C-0336A-2013) were carried out in 2013 April in service mode with the Swedish heterodyne receiver instrument APEX-3 (Vassilev et al. 2008) tuned to 413.1 GHz in the upper sideband. The receiver was connected to the XFFTS spectrometer covering the entire receiver band with a spectral resolution of 0.076 kHz, corresponding to a velocity resolution of 0.055 km s^{-1} at this frequency. During the observing runs, the amount of precipitable water vapour was mostly between 0.8 and 1.2 mm, resulting in system temperatures between 400 and 500 K depending on source elevation. Because the NHD signal is expected to be moderately extended, the position switching mode was used with an offset of 70 arcsec in right ascension to the West of the source, in a direction where the density of the protostellar envelope and the molecular emission drops quickly (Castets et al. 2001). The data were reduced using the GILDAS/CLASS software[3]: the spectra were averaged together and a low-order polynomial was fitted to line-free regions of the spectra and subtracted. The forward efficiency of the antenna was taken to be 0.95 and the beam efficiency 0.65, an intermediate value between the measured value at 352 GHz and that measured at 464 GHz (Güsten et al. 2006). These efficiencies were used to convert the spectra from the T_a^* to the T_{mb} scale. The APEX beam size is 15 arcsec full width at half-maximum (FWHM) at the observing frequency. The rms noise in the spectrum is ∼ 33 mK (T_{mb} scale) in 0.11 km s^{-1} channels.

2.3 ND_2 observations

The search for doubly deuterated amidogen was carried out with the *Herschel Space Observatory* (Pilbratt et al. 2010) in the course of an open time project (PI: P. Hily-Blant, OBSID 1342227404). The ND_2 $N_{K_aK_c}J$: 1_{11} 1/2–0_{00} 1/2 line at 531 GHz was observed with the HIFI instrument (de Graauw et al. 2010) in band 1a on 2011 August 26 (OBSIDs 1342227403 and 1342227404), with both the wide band spectrometer (WBS), and the high-resolution spectrometer (HRS). The WBS has a spectral resolution of 1.1 MHz, corresponding to a velocity resolution of 0.6 km s^{-1} at the frequency of the observations, and the HRS has a resolution of 0.25 MHz, corresponding to a velocity resolution of 0.14 km s^{-1}. The observations were performed in the single pointing dual beam switch mode with fast chopping (4 Hz) and optimization of the continuum. This improves the subtraction of the standing waves and the determination of the continuum. In this mode, the OFF positions are at fixed offsets 3 arcmin away from the source coordinates on either side (East–West) of the source. We checked on the spectra of these OFF positions that no ND_2 signal was present. The data were processed with the HIPE pipeline (Ott 2010) version 14 up to level 2.5 products, after which they were exported to GILDAS/CLASS data format for further analysis: the spectra in both horizontal and vertical polarizations were averaged, and a first-order polynomial baseline was fitted to line-free regions of the spectrum and subtracted. The HIFI beam at 531 GHz, the frequency of the ND_2 transitions, is ∼39 arcsec FWHM, the main beam efficiency η_{mb} is 0.62 and the forward efficiency η_{fwd} is 0.96

[2]This publication is based on data acquired with the Atacama Pathfinder Experiment (APEX). APEX is a collaboration between the Max-Planck-Institut fur Radioastronomie, the European Southern Observatory, and the Onsala Space Observatory.
[3]http://www.iram.fr/IRAMFR/GILDAS

(Shipman et al. 2017). The rms noise in the spectrum is ∼6.6 mK (T_{mb} scale) in 0.56 km s^{-1} channels.

2.4 Continuum data

In this study, we also used continuum data (see Section 3.1). Maps at 250, 350, and 500 μm observed by *Herschel*/SPIRE (Griffin et al. 2010) were taken from the *Herschel* Gould Belt survey (HGBS André et al. 2010). We used the level 2.5 maps of the L1689 cloud (OBSID 1342239773) processed by the HIPE pipeline (version 12.0) and calibrated for extended sources. Absolute calibration using HFI data from the *Planck* satellite is also performed by the pipeline. We also subtracted from the images a constant offset measured in an apparently emission-free region to the South-East of the L1689 cloud. This serves as a first-order removal of the emission from the diffuse galactic background. Because the *Herschel*/SPIRE maps focus on a ∼15 arcmin × 15 arcmin region centred on IRAS16293−2422 and do not include areas outside of the Rho Ophiuchi cloud, we used the larger scale maps of Rho Ophiuchi covering the whole complex (OBSID 1342205093 and 1342205094, also part of the HGBS) to measure the off-cloud emission for each of the three wavelengths. These values were corrected from the intensity offsets between the small maps of IRAS16293−2422 and the large-scale maps of Rho Ophiuchi by comparing the map intensities in a region common to both types of maps. The beam sizes (FWHM) at wavelengths 250, 350, and 500 μm are 18, 25, and 36 arcsec, respectively. As in Bacmann et al. (2016), additional ground-based maps of the region at 850 μm taken with the SCUBA-2 bolometer array on the James Clark Maxwell Telescope (JCMT) as part of the JCMT Gould Belt Survey (Holland et al. 2013) were used. The data and the data reduction procedure are described in Pattle et al. (2015). Finally, we also used the map at 1.2 mm taken by Lis et al. (2002a) with the MAMBO-II bolometer on IRAM 30 m telescope. The FWHM beam sizes are ∼14 arcsec for the JCMT/SCUBA-2 map and ∼11 arcsec for the IRAM 30 m data.

3 RESULTS AND ANALYSIS

3.1 Continuum estimation

3.1.1 NHD

Because the ground-based observations do not enable us to measure the continuum level of the NHD spectrum, we use available continuum observations taken at various wavelengths to infer the value at the frequency of the NHD transition (413 GHz, which corresponds to a wavelength of 726 μm) by interpolation. At wavelengths larger than typically 200 μm, the spectral energy distribution of the protostar is close to the Rayleigh–Jeans regime, so that fitting a simple power law to the source fluxes as a function of wavelength allows for a straightforward determination of the continuum value at 413 GHz. First the continuum maps were smoothed to a common angular resolution, i.e. 36 arcsec, that of the coarsest map from SPIRE at 500 μm. To achieve this, the 250, 350, and 500 μm SPIRE maps were convolved with the appropriate kernels provided by Aniano et al. (2011). The 850 μm SCUBA-2 map and the 1.2 mm MAMBO-II map were convolved with Gaussian kernels of FWHM 33 and 34.3 arcsec, respectively, the former also from Aniano et al. (2011). The average surface brightnesses of the source at each wavelength were measured in an aperture of 15 arcsec, corresponding to the beam of the NHD observations. We also added the continuum intensity from the *Herschel*/HIFI ND_2 spectrum at 531 GHz (565 μm), which is at a similar resolution. A power law of index $\alpha = -2.6$ could be fitted to the data points (Fig. 1), which enabled us to interpolate the intensity at 413 GHz at a resolution of 36 arcsec. To derive the source intensity at the resolution of the APEX observations (15 arcsec), we smoothed the SCUBA-2 map to the resolution of the APEX observations by convolution with a Gaussian kernel of 5 arcsec from Aniano et al. (2011), and the MAMBO-II bolometer map by convolution with a Gaussian kernel of 10.2 arcsec FWHM. Those two points were fitted with a power law with the same exponent α, and from this power law, the value of the surface brightness was obtained at 413 GHz at a resolution of 15 arcsec. This method assumes that the dust opacity index does not depend on the angular resolution, i.e. on the dust temperature or density in the ranges probed by the observations. While this might not be true in the general case, this approximation is good enough for our purpose here, considering the uncertainties in the data analysis. The interpolated surface brightness is 3154 MJy sr^{-1}, corresponding to a brightness temperature T_c(NHD) = 600 mK. We used the latter value as the continuum brightness temperature of the source in the APEX spectrum.

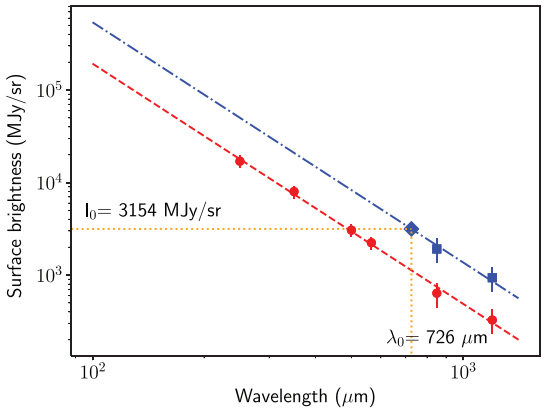

Figure 1. Continuum intensities of IRAS16293−2422 measured at 36 arcsec resolution (red dots) and power-law fit (red dashed line). The index of the power law is found to be $\alpha = -2.6$. The blue squares are the intensities at 15 arcsec resolution, and the blue dash–dotted line fits these points with the same power-law index α. The derived intensity I_0 at the wavelength of the APEX observations ($\lambda_0 = 726$ μm) and at a resolution of 15 arcsec is marked as a blue diamond.

Because of the observing technique used to remove the strong atmospheric emission for ground-based observations, the emission arising from extended structures in the astrophysical source is partly filtered out. Since we are interested in the mean intensity of the protostar in a compact region around its maximum, our surface brightness values at 850 μm and 1.2 mm should not be too affected. Nevertheless, the filtering of the extended emission for the JCMT and IRAM 30 m maps could lead to an underestimate of the surface brightness at 850 μm and 1.2 mm. Therefore, the power law that we fitted could in fact be shallower and the continuum intensity at 413 GHz could be slightly overestimated.

3.1.2 ND_2

For ND_2, the continuum was measured by fitting a zeroth-order polynomial to the spectrum in regions that do not show any spectral lines. Assuming that the observed continuum is the sum of that in the upper sideband and that in the lower sideband, and supposing that it increases with frequency following a power law of index $\alpha = -2.6$,

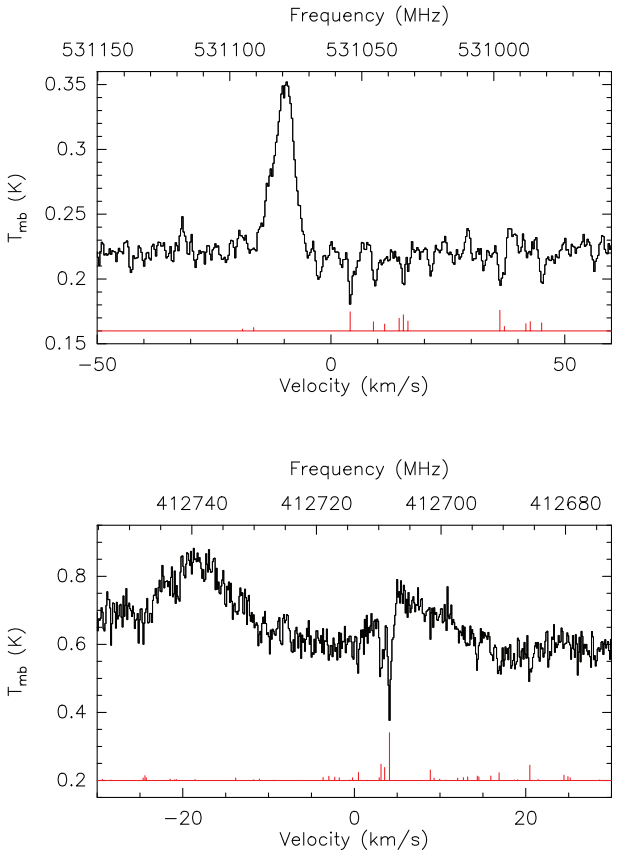

Figure 2. NHD (bottom panel) and ND_2 (top panel) spectra in IRAS16293−2422. The red sketch shows the positions and expected relative intensities of the hyperfine components. The strong emission feature at a velocity of −10 km s^{-1} (corresponding to a frequency of 531079.2 MHz) in the ND_2 spectrum is likely the $N_{K_aK_c}: 11_{1\,11}$–$10_{1\,10}$ transition of CH_3OH. The broad features in the NHD spectrum at velocities −17 and 7 km s^{-1} are unidentified.

we find that the single sideband continuum at 531 GHz is $T_c(ND_2) = 210$ mK.

3.2 NHD and ND_2 spectra

The observed NHD and para-ND_2 spectra are shown in Fig. 2. For both spectra, the continuum levels derived in Section 3.1 were added to the spectra after baseline withdrawal. Both molecules are seen in absorption against the continuum. For the NHD spectrum, a rather broad emission feature (rest frequency 412702.5 MHz) is visible at a similar velocity as that of the NHD lines. The FWHM of this feature is ∼8.5 km s^{-1}, like for other similarly looking features in the spectrum. Such wide spectral lines have already been seen in this source (e.g. TIMASSS, Caux et al. 2011), and are consistent with that of lines emitted in the hotter central region. However, these broad emission lines unlikely arise from NHD itself: the near-Gaussian feature against which the two strongest NHD features are seen in absorption peaks at a velocity ∼6.5 km s^{-1}, higher than the hot corino velocity at 3.1 and 2.7 km s^{-1} for sources A and B, respectively (Jørgensen et al. 2011, 2016), and than the line velocities measured in the TIMASSS survey (lower than 5 km s^{-1}). In the following, we have considered that this feature arises from an unknown molecular transition (different from NHD), but we cannot fully exclude the possibility that it is a baseline ripple. The other strong, broad emission lines seen in Fig. 3 (e.g. at 412738.7, 413541.1, and 413564.9 MHz) are also unidentified and probably arise from the warm inner region.

Several hyperfine components are detected with the expected velocity shifts both for NHD (J: 3/2−1/2) at 412.7 GHz and para-ND_2 at 531 GHz. No hyperfine component is seen for the NHD J: 1/2−1/2 transition at 413.5 GHz (Fig. 3). The source velocity is found to be 4.1 km s^{-1} for both NHD and ND_2. This is about 0.3 km s^{-1} higher than the velocities of 3.8 km s^{-1} for ND, NH and NH_2 in the same source (Bacmann et al. 2010; Hily-Blant et al. 2010), hinting at possibly different spatial locations for the deuterated forms of amidogen, or a lack of accuracy in the values of the rest frequencies. Because the noise in the spectra is relatively high, only the hyperfine components that are expected to be the strongest are detected, and no theoretically weak component is detected, so that we are confident that both species are present.

The fact that the lines are seen in absorption and their narrow linewidths ($\Delta v = 0.5$ km s^{-1} for NHD and $\Delta v \sim 0.7$ km s^{-1} for ND_2, though the latter value is subject to more uncertainty because of the lower signal-to-noise ratio) is consistent with the presence of both species in the low-density and low-temperature protostellar envelope, rather than in the higher density regions close to the hot core.

3.3 Column density estimates

Both NHD and ND_2 spectra were analysed in a similar fashion: the optical depth was derived as a function of frequency given a column density and assuming the same excitation temperature for all the hyperfine components. Because of the overlap between the hyperfine components, such a simple model may not be able to reproduce well the line relative ratios. More sophisticated and accurate treatments are not possible, since collisional coefficients are not yet available for these two species. The consequence on the column density determination should remain limited because of the low optical depths of the transitions. For Gaussian lines, the velocity-integrated optical depth is

$$\int \tau(v)\mathrm{d}v = \tau_0 \Delta v \sqrt{\frac{\pi}{4\ln(2)}},$$

where τ_0 is the line central optical depth and Δv the line FWHM. The optical depth at line centre is therefore given by

$$\tau_0 = N \frac{c^3}{8\pi\nu^3} \frac{A_{\rm ul} g_{\rm up}}{Q(T_{\rm ex})} \frac{e^{h\nu/(k_{\rm b}T_{\rm ex})} - 1}{e^{E_{\rm up}/(k_{\rm b}T_{\rm ex})}} \frac{1}{\Delta v} \sqrt{\frac{4\ln(2)}{\pi}},$$

where $Q(T_{\rm ex})$ is the partition function at excitation temperature $T_{\rm ex}$, N is the total molecular column density, ν the frequency of the transition, $A_{\rm ul}$ the Einstein spontaneous emission coefficient of the transition, $g_{\rm up}$ the upper level degeneracy, c the speed of light, $E_{\rm up}$ the energy of the upper level, and h and $k_{\rm b}$ are the Planck and Boltzmann constants, respectively. The total optical depth as a function of velocity is given by (neglecting the effect of line overlap on line excitation)

$$\tau(v) = \sum_i \tau_0^i \exp\left(-4\ln(2)\left(\frac{v - v_0}{\Delta v}\right)^2\right),$$

where v_0 is the rest velocity, i refers to hyperfine component i and τ_0^i the optical depth of the hyperfine component i is $\tau_0^i = \tau_0 R_i$, with R_i the hyperfine component statistical weight. The brightness temperature is then simply

$$T_{\rm b}(v) = (J_\nu(T_{\rm ex}) - J_\nu(T_{\rm CMB}))(1 - e^{-\tau(v)}) + T_{\rm c}\, e^{-\tau(v)},$$

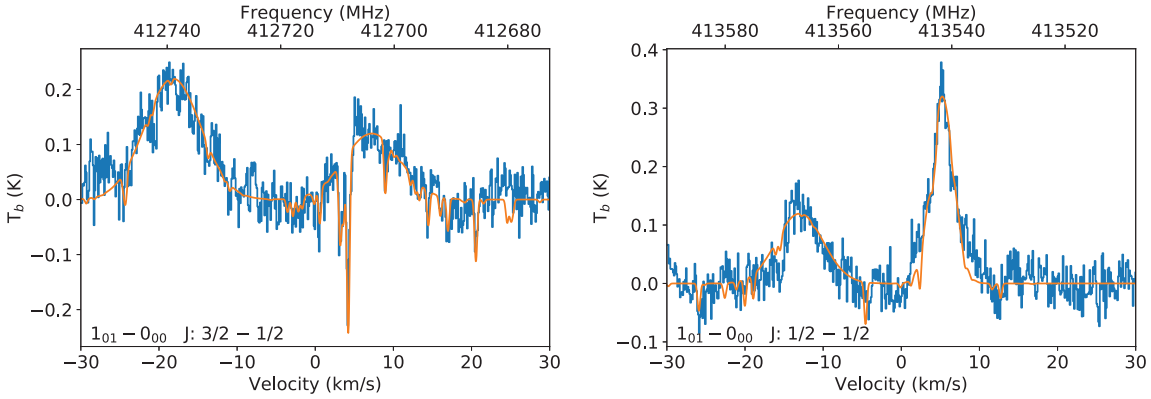

Figure 3. NHD spectra for the *J*: 3/2–1/2 (left-hand panel) and *J*: 1/2–1/2 (right-hand panel) transitions (blue line) and model spectra (red line). The broad emission features at 412702.5, 412738.7, 413541.1, and 413564.9 MHz are unidentified molecular lines probably originating in the warm inner regions.

with $J_\nu(T)$ the Rayleigh–Jeans equivalent temperature, $T_{\rm CMB}$ the temperature of the cosmic microwave background ($T_{\rm CMB} = 2.73$ K) and $T_{\rm c}$ the continuum temperature ($T_{\rm c} = 600$ mK for NHD and $T_{\rm c} = 210$ mK for ND_2, see Section 3.1).

The observed spectra were then fitted by adjusting the value of the column density, having assumed an excitation temperature. We assumed an excitation temperature of 3 K, but the influence on the column density value is basically unchanged for an excitation temperature range of 2.8−4 K. This is a reasonable assumption for lines seen in absorption, however from our spectra we cannot fully exclude higher values of $T_{\rm ex}$, which would lead to the need for higher column densities to fit the spectra. For excitation temperatures larger than 5.3 K for ND_2 and 5.8 K for NHD, the lines would be seen in emission. For NHD, we assumed that the line is seen in absorption against a background varying with velocity and made of the dust continuum and a line possibly originating from the hot core with an FWHM linewidth of 8.5 km s^{-1}.

With $T_{\rm ex} = 3$ K, we find column densities of $N \sim 3.9 \times 10^{13}$ cm^{-2} for NHD and $N \sim 7 \times 10^{12}$ cm^{-2} for para-ND_2. For these column density values, the maximum optical depth is 0.5 for the components of NHD and 0.3 for those of ND_2. Assuming an ortho-to-para ratio of 0.4 for ND_2, consistent with the ortho-to-para ratio derived from the observations of Melosso et al. (2020), we find that the total (ortho + para) ND_2 column density is $\sim 10^{13}$ cm^{-2}. Note that in the case of NH_2 the excitation temperature could be determined from the relative ratios of the hyperfine components because of the high signal-to-noise ratio of the spectra, and was found to be ~ 9 K (Hily-Blant et al. 2010).

We note that the critical densities associated with the detected transitions are $\gtrsim 10^6$ cm^{-3} assuming collisional rate coefficients for NHD and ND_2 of a few 10^{-11} cm^{3}s^{-1} (see Bouhafs et al. 2019, for the main isotopologue NH_2). Excitation temperatures are therefore expected to be lower than the kinetic temperature in the protostellar envelope where $T_{\rm kin} \sim 10$ K and $n \sim 10^5$ cm^{-3}, but will depend on the exact physical conditions of the absorbing molecules.

Acceptable fits are found for N(NHD) $\sim 3.2 \times 10^{13}$ to 4.7×10^{13} cm^{-2} and we adopt this range for the uncertainty on the NHD column density value. Uncertainties on the para-ND_2 column density value are $\sim 5 \times 10^{12}$ to 8×10^{12} cm^{-2}. The fits are shown in Figs 3 and 4 for NHD and ND_2, respectively.

As mentioned before, we cannot exclude that the signal against which the NHD transitions are seen is due to atmospheric fluctuations (i.e. foreground emission). Assuming this is the case, we first withdrew a high-order (e.g. 9) polynomial to the spectrum, excluding only the NHD absorption features from the fit, after which we proceeded with fitting the spectrum as described above. In this case, and assuming an excitation temperature of $T_{\rm ex} = 3$ K as well, the NHD column density needed to fit the absorption feature is $N \sim 4.6 \times 10^{13}$ cm^{-2}. This is within the uncertainties of our previous NHD column density determination.

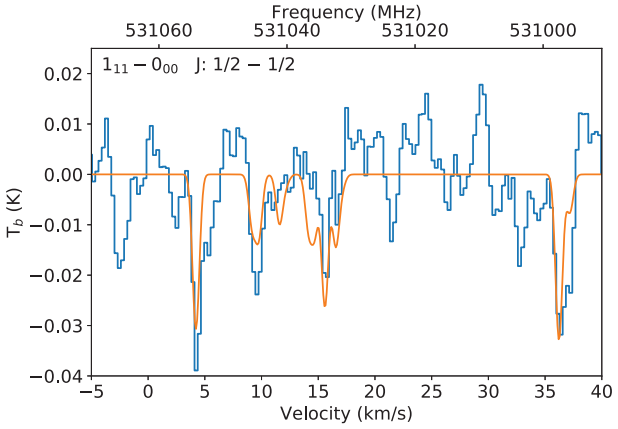

Figure 4. ND_2 spectrum for the J: 1/2–1/2 transition (blue line) and model spectrum (red line).

Table 1 sums up the observed column densities for ortho-NH_2, NHD and para-ND_2. These values are consistent with the ones derived by Melosso et al. (2020). Note that for the designation of spin symmetries, we have followed the standard Maue's rule (Maue 1937) where the ortho species have the largest statistical weight and para species have the smallest statistical weight. Thus, in the case of ND_2, the symmetric rotational levels ($K_{\rm a} + K_{\rm c}$ even) combine with antisymmetric nuclear spin function $I_{\rm D} = 1$ i.e. para states, while antisymmetric rotational levels ($K_{\rm a} + K_{\rm c}$ odd) combine with symmetric nuclear spin function $I_{\rm D} = 0$, 2, i.e. ortho states. The reverse convention was employed in Melosso et al. (2020, see their appendix A.2), hence our value of column density for para-ND_2 should be compared with their value for ortho-ND_2.

3.4 Abundance ratios

Hily-Blant et al. (2010) observed ortho-NH_2 at the same position in IRAS16293−2422. Based on this observation, and assuming an ortho-to-para ratio of 2, close to the value suggested by their model, Le Gal et al. (2014) derived a total (ortho+para) NH_2 column density

Table 1. Comparison between chemical model predictions at a central density of 10^7 cm^{-3}, and observational constraints for the column density of ortho-NH_2, NHD, and para-ND_2. The model values are for the envelope. Also given are the ortho-to-para ratios and total column densities for NH_2 and ND_2 as obtained with the UGAN model. The last column sums up the observational values from the work by Melosso et al. (2020).

Species	Model (cm^{-2})	Observation (this work) (cm^{-2})	Melosso et al. (2020) (cm^{-2})
ortho-NH_2	2.9×10^{13}	5.0×10^{13}	5.4×10^{13}
para-NH_2	1.5×10^{13}		
NHD	3.2×10^{13}	3.9×10^{13}	4.7×10^{13}
ortho-ND_2	3.8×10^{12}		2.4×10^{12}
para-ND_2	1.2×10^{12}	7.0×10^{12}	6.6×10^{12}
NH_2	4.4×10^{13}		
ND_2	5.0×10^{12}		
ortho-NH_2/para-NH_2	1.9		
ortho-ND_2/para-ND_2	3.1		0.4
NH_2/ND_2	8.7		
NHD/ND_2	6.4		

of 7.5×10^{13} cm^{-2}, which we adopt here. This leads to relative column density ratios NH_2:NHD:ND_2 of ∼8:4:1.

Large ratios between singly deuterated molecules and main isotopologues of a few 10 per cent such as we find here for NHD/NH_2 are common in protostellar envelopes, for molecules formed in the later stages of prestellar evolution (e.g. formaldehyde, methanol, or ammonia, but unlike water, see Taquet et al. 2013), although the case of the amidogen radical presented here is rather extreme. For example in IRAS16293−2422, HDCO/H_2CO is 13−16 per cent (Loinard et al. 2000), CH_2DOH/CH_3OH is 10−50 per cent (Parise et al. 2004) and NH_2D/NH_3 is 10 per cent (van Dishoeck et al. 1995). For ammonia, Roueff et al. (2005) have compiled NH_2D/NH_3 ratios between 10 per cent and 30 per cent in a sample of sources made of dense cores and protostars. Such fractionation ratios can usually be accounted for by present chemical models (e.g. Aikawa et al. 2012; Roueff et al. 2015).

The high abundance of ND_2 is reminiscent of other molecules, for which it has been observed that doubly deuterated species were often overabundant. Indeed, the ratio between the doubly and the singly deuterated isotopomers is in some species even larger than the ratio between the singly deuterated and the main isotopologue. In IRAS16293−2422, D_2CO/HDCO is 30−40 per cent (Loinard et al. 2000), i.e. two to three times higher than HDCO/H_2CO. Other protostellar envelopes are also characterized by D_2CO/HDCO ratios which are higher than HDCO/H_2CO ratios (Parise et al. 2006) (see also the D_2CO/HDCO measurement in the cloud ρ Oph A by Bergman et al. 2011). For ammonia and methanol, the ratios XD_2/XHD (where X represents the species) are of the same order (though slightly lower) as the XHD/XH_2 ratios (Roueff et al. 2005; Parise et al. 2006). Water is also characterized by high abundances of its doubly deuterated isotopologue, with D_2O/HDO > HDO/H_2O in the envelope of IRAS16293−2422, as reported by Coutens et al. (2013). Moreover, high angular resolution interferometric observations sampling the warm inner regions of young protostars show very high abundances of doubly deuterated molecules: in NGC 1333−IRAS2, D_2O/HDO is found to be seven times higher than HDO/H_2O (Coutens et al. 2014). Other species like formaldehyde, observed with ALMA in the hot core of IRAS16293−2422 (Persson et al. 2018) or doubly deuterated methyl formate, which was recently detected in the hot core of IRAS16293−2422 (Manigand et al. 2019) similarly show XD_2/XHD ratios typically two to three times higher than the XHD/XH_2 ratio. So far, chemical models have struggled to explain this feature.

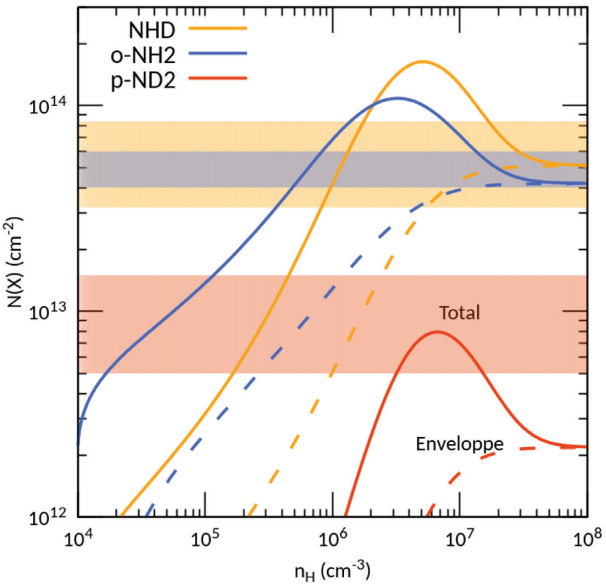

Figure 5. Model predictions (Hily-Blant et al. 2018) showing the predicted column densities of NH_2, NHD, and ND_2 as a function of core density (see the text). The dashed lines represent the column density of the envelope, while the solid lines represent the total (core + envelope) column density. The shaded rectangles show the observed column densities.

4 CHEMICAL MODEL

We compare the observed column densities with the predictions of the gas-grain chemical model presented in Hily-Blant et al. (2018). The model is based on the University of Grenoble Astrochemical Network (UGAN), which includes the nuclear-spin states of H_2, H_2^+, H_3^+ and of all the carbon, nitrogen, oxygen, and sulphur containing hydrides, as well as their abundant deuterated forms. Grain-surface reactions are not explicitly included in the UGAN network, except the formation (and immediate desorption) of H_2 and isotopologues. The rates of adsorption and desorption and the list of species assumed to form in grain mantes can be found in Hily-Blant et al. (2018). In this model, nitrogen hydrides are formed exclusively by gas-phase reactions.

An update of the oxygen hydrides chemistry was recently performed by Faure et al. (2019). The dynamical model is presented in Hily-Blant et al. (2018) and is inspired from the studies of gravitational collapse by Larson (1969) and Penston (1969). Briefly, the core, which is considered to have a constant density central plateau surrounded by an enveloppe of density falling as r^{-2}, where r is the radius, collapses self-similarly. The density of the central plateau is homogeneous and increases with time while its contribution to the total mass and total radius (and therefore total column density) decreases with time. Full details can be found in Hily-Blant et al. (2018). The model was run for a kinetic temperature fixed at $T = 10$ K and an initial core density $n_H = 10^4$ cm^{-3}. Other parameters can be found in table 1 of Hily-Blant et al. (2018, 'reference' model).

The total column density for ortho-NH_2, NHD, and para-ND_2, and the contribution of the envelope, are shown as a function of the core density in Fig. 5, where the observational error bars include

the uncertainty on the excitation temperatures. As may be seen, the contribution of the central plateau to the total column density reaches a maximum at a central density $n_H \approx 3-6 \times 10^6$ cm^{-3}, and is then negligible above typically 5×10^7 cm^{-3}. Incidentally, at an evolution time of the cloud corresponding to a central density of $n_H \approx 6.5 \times 10^6$ cm^{-3}, the column densities of the envelope derived from the model are 2.7×10^{13} and 2.5×10^{13} cm^{-2}, for ortho-NH_2 and NHD, respectively. Although the model agrees with the observational constraints at this stage of cloud evolution, very good agreement is obtained also at central densities above 10^7 cm^{-3}, while the contribution of the plateau is already mitigated. For para-ND_2, on the other hand, the total (core + envelope) column density matches the observation values at $n_H = 6.5 \times 10^6$ cm^{-3}. At larger core densities (where the envelope dominates) the model underestimates the observational value by a factor of ∼2−3. It may be emphasized that, on observational grounds, the detected molecules most likely belong to the envelope for at least two reasons: lines are seen in absorption, and also, because the diameter of the inner plateau is 10^3 au, or 7 arcsec (at a distance of 140 pc; Dzib et al. 2018) when n_H reaches 6.5×10^5 cm^{-3}. As a result, while our model can reproduce the column density of ortho-NH_2 and NHD within a factor of 2, it is found to underestimate that of para-ND_2 by a factor larger than 2. At a central density of 10^7 cm^{-3}, the abundance ratios are 8.7:6.4:1 for NH_2:NHD:ND_2, with ortho-NH_2/para-NH_2 = 1.9 and ortho-ND_2/para-ND_2 = 3.1. We also note that the ortho-to-para ratio of NH_2 stays very close to 2 throughout the collapse, while that of ND_2 increases steadily from 2.1 to 3.1. While the above successive deuteration ratios taking into account the total (ortho+para) column densities of NH_2 and ND_2 agree with our observations to within a factor of 2 (see Table 1), our model has trouble reproducing such a low ortho-to-para ratio of ND_2 as found by Melosso et al. (2020). This possibly suggests that some thermalization reactions are missing in our UGAN network, since the measured ortho-to-para ratio corresponds to a spin temperature as low as 5−6 K.[4] Finally, our model predicts that the NH_2:NHD:ND_2 ratios remain constant and equal to 7.1:5.6:1 above a density of 3×10^7 cm^{-3}.

These results indicate that pure gas-phase chemistry as in the UGAN model can reproduce the observed column densities and abundance ratios of the amidogen radical isotopologues in protostellar envelopes within a factor of ∼2–3. We note, however, that we have assumed identical rate coefficients for dissociative recombination of all deuterated isotopologues of NH_4^+ with, in addition, statistical H/D branching ratios for the products. These assumptions are questionable because dissociative recombination experiments have suggested the occurence of isotope effects (e.g. Öjekull et al. 2004). This will be investigated in a future, more complete, modelling study.

Statistical distributions of deuterium atoms is expected if nitrogen hydrides form by successive hydrogenations of nitrogen atoms on grain surfaces (Tielens & Hagen 1982; Brown & Millar 1989; Charnley, Tielens & Rodgers 1997). According to the grain-surface addition scheme, NHD/NH_2 = 2 D/H (where D/H denotes the *atomic* D over H ratio) and ND_2/NH_2 = (D/H)^2. This leads to ND_2/NHD = 0.25 NHD/NH_2. This value is consistent with the observed ratios, for which ND_2/NHD = 1/2 NHD/NH_2 within a factor of 2. Therefore, although grain-surface chemistry is not needed to account for the observed abundances of these species, we cannot exclude grain-surface processes either. We note that the ortho-to-para ratios provide additional constraints but current measurements have large uncertainties (Harju et al. 2017; Hily-Blant et al. 2018; Melosso et al. 2020). Indeed, taking the ortho-to-para ratio for ND_2 as 3 as indicated by our chemical model in the late collapse stages, we find a total ND_2 column density of 4.8×10^{13} cm^{-2}. This in turn leads to ND_2/NHD = 4/3 NHD/NH_2, with which the statistical grain-surface scenario is inconsistent.

Our analysis and chemical model are based on the hypothesis that all species are coexistent. However, in the case of NH and ND, a detailed radiative transfer model of the spectra of these two species seen towards the dense core IRAS16293E showed that the signal from NH and that from ND came from spatially separate regions (Bacmann et al. 2016), with the ND transition sampling higher density material. It is possible as well that in the case of amidogen, the deuterated isotopologue is concentrated at higher densities than NH_2, and even more so for the doubly deuterated isotopologue. Indeed deuteration proceeds faster at higher densities because it is tightly linked to the depletion of abundant gas-phase species like CO. The discrepancy between the model and the ND_2 observations could also indicate that important fractionation reactions are missing from the model.

In order to assess the sensitivity of our results to the assumed excitation temperature, we have derived the column densities assuming T_{ex} = 4.5 K. With this value, we find N(NHD) = 7×10^{13} cm^{-2} and N(para-ND_2) = 1.2×10^{13} cm^{-2}, i.e. a total (ortho+para) column density of ND_2 $N(ND_2) = 1.7 \times 10^{13}$ cm^{-2}, assuming as before an ortho-to-para ratio of 0.4 for ND_2. While for NH_2, the excitation temperature could be determined by fitting the relative ratios of the hyperfine components (Hily-Blant et al. 2010), this is not possible for NHD and ND_2 because of the low signal-to-noise ratio of the observations. With these column density values, the relative ratios between the different amidogen isotopologues are 4:4:1 for NH_2:NHD:ND_2. Clearly, a non-LTE model is required in order to derive more accurate column densities and abundance ratios. This will be performed in a forthcoming paper thanks to the next availability of collisional rate coefficients for NHD and ND_2 (Bop et al., in preparation).

5 CONCLUSIONS

We have detected the singly deuterated and doubly deuterated isotopologues of amidogen, NHD and para-ND_2 towards the envelope of the class 0 protostar IRAS16293−2422. The column densities of NHD and para-ND_2 are estimated to be 3.2×10^{13} to 7×10^{13} cm^{-2} and 5×10^{12} to 1.2×10^{13} cm^{-2}, respectively. The observed relative ratios between the deuterated isotopologues and the main isotopologue NH_2 can be reproduced within a factor of 2−3 with our pure gas-phase chemical model. This result adds to previous evidence that pure gas-phase chemistry can reproduce many features (i.e. spin-state ratios for NH_2, deuterium fractionation, abundances) observed in nitrogen hydrides (Hily-Blant et al. 2018). However, the data are also consistent with the statistical ratios expected from grain-surface chemistry. A more elaborate analysis of the observations is necessary taking into account the different angular resolutions for NHD and ND_2 as well as likely non-LTE excitation effects. A better understanding of the ortho-to-para ratio in ND_2 might help to distinguish between both chemical routes.

ACKNOWLEDGEMENTS

This research has made use of data from the *Herschel* Gould Belt survey (HGBS) project (http://gouldbelt-herschel.cea.fr). The HGBS is a *Herschel* Key Programme jointly carried out by SPIRE Specialist

[4]We note that at temperatures below ∼10 K, the ortho-to-para ratio of ND_2 can be approximated by the function $6 \times \exp(-15.5/T_{spin})$.

Astronomy Group 3 (SAG 3), scientists of several institutes in the PACS Consortium (CEA Saclay, INAF-IFSI Rome and INAF-Arcetri, KU Leuven, MPIA Heidelberg), and scientists of the *Herschel* Science Center (HSC). This work has been supported by the Agence Nationale de la Recherche (ANR-HYDRIDES), contract ANR-12-BS05-0011-01. This work was supported by the Programme National 'Physique et Chimie du Milieu Interstellaire' (PCMI) of INSU,CNRS with INC/INP co-funded by CEA and CNES.

DATA AVAILABILITY

The data underlying this article were accessed from the ESO archive (APEX data) and The *Herschel Space Observatory* archive (HIFI/*Herschel* data).

REFERENCES

Aikawa Y., Wakelam V., Hersant F., Garrod R. T., Herbst E., 2012, ApJ, 760, 40
André P. et al., 2010, A&A, 518, L102
Aniano G., Draine B. T., Gordon K. D., Sandstrom K., 2011, PASP, 123, 1218
Bacmann A. et al., 2010, A&A, 521, L42
Bacmann A. et al., 2016, A&A, 587, A26
Bergman P., Parise B., Liseau R., Larsson B., 2011, A&A, 527, A39
Bouhafs N., Bacmann A., Faure A., Lique F., 2019, MNRAS, 490, 2178
Brown P. D., Millar T. J., 1989, MNRAS, 240, 25P
Castets A., Ceccarelli C., Loinard L., Caux E., Lefloch B., 2001, A&A, 375, 40
Caux E. et al., 2011, A&A, 532, A23
Charnley S. B., Tielens A. G. G. M., Rodgers S. D., 1997, ApJ, 482, L203
Coutens A. et al., 2013, A&A, 553, A75
Coutens A., Jørgensen J. K., Persson M. V., van Dishoeck E. F., Vastel C., Taquet V., 2014, ApJ, 792, L5
de Graauw T. et al., 2010, A&A, 518, L6
Dumouchel F., Kłos J., Toboła R., Bacmann A., Maret S., Hily-Blant P., Faure A., Lique F., 2012, J. Chem. Phys., 137, 114306
Dzib S. A. et al., 2018, A&A, 614, A20
Faure A., Hily-Blant P., Rist C., Pineau des Forêts G., Matthews A., Flower D. R., 2019, MNRAS, 487, 3392
Griffin M. J. et al., 2010, A&A, 518, L3
Güsten R., Nyman L. Å., Schilke P., Menten K., Cesarsky C., Booth R., 2006, A&A, 454, L13
Harju J. et al., 2017, A&A, 600, A61
Hily-Blant P. et al., 2010, A&A, 521, L52
Hily-Blant P., Faure A., Rist C., Pineau des Forêts G., Flower D. R., 2018, MNRAS, 477, 4454
Holland W. S. et al., 2013, MNRAS, 430, 2513
Jørgensen J. K., Bourke T. L., Nguyen Luong Q., Takakuwa S., 2011, A&A, 534, A100
Jørgensen J. K. et al., 2016, A&A, 595, A117
Kanada M., Yamamoto S., Saito S., 1991, J. Chem. Phys., 94, 3423
Kobayashi K., Ozeki H., Saito S., Tonooka M., Yamamoto S., 1997, J. Chem. Phys., 107, 9289
Larson R. B., 1969, MNRAS, 145, 271
Le Gal R., Hily-Blant P., Faure A., Pineau des Forêts G., Rist C., Maret S., 2014, A&A, 562, A83
Linsky J. L. et al., 2006, ApJ, 647, 1106
Lis D. C., Gerin M., Phillips T. G., Motte F., 2002a, ApJ, 569, 322
Lis D. C., Roueff E., Gerin M., Phillips T. G., Coudert L. H., van der Tak F. F. S., Schilke P., 2002b, ApJ, 571, L55
Loinard L., Castets A., Ceccarelli C., Tielens A. G. G. M., Faure A., Caux E., Duvert G., 2000, A&A, 359, 1169
Manigand S. et al., 2019, A&A, 623, A69
Maue A. W., 1937, Ann. Phys., 422, 555
Melosso M., Degli Esposti C., Dore L., 2017, ApJS, 233, 15
Melosso M. et al., 2020, A&A, 641, A153
Motoki Y., Ozeki H., Kobayashi K., 2013, 68th International Symposium on Molecular Spectroscopy. p. ETH01
Öjekull J. et al., 2004, J. Chem. Phys., 120, 7391
Ott S., 2010, in Mizumoto Y., Morita K. I., Ohishi M., eds, ASP Conf. Ser. Vol. 434, Astronomical Data Analysis Software and Systems XIX. Astron. Soc. Pac., San Francisco, p. 139
Pagani L., Salez M., Wannier P. G., 1992, A&A, 258, 479
Parise B., Castets A., Herbst E., Caux E., Ceccarelli C., Mukhopadhyay I., Tielens A. G. G. M., 2004, A&A, 416, 159
Parise B., Ceccarelli C., Tielens A. G. G. M., Castets A., Caux E., Lefloch B., Maret S., 2006, A&A, 453, 949
Pattle K. et al., 2015, MNRAS, 450, 1094
Penston M. V., 1969, MNRAS, 144, 425
Persson M. V. et al., 2018, A&A, 610, A54
Pilbratt G. L. et al., 2010, A&A, 518, L1
Roberts H., Herbst E., Millar T. J., 2003, ApJ, 591, L41
Roueff E., Lis D. C., van der Tak F. F. S., Gerin M., Goldsmith P. F., 2005, A&A, 438, 585
Roueff E., Loison J. C., Hickson K. M., 2015, A&A, 576, A99
Shipman R. F. et al., 2017, A&A, 608, A49
Taquet V., Peters P. S., Kahane C., Ceccarelli C., López-Sepulcre A., Toubin C., Duflot D., Wiesenfeld L., 2013, A&A, 550, A127
Tielens A. G. G. M., Hagen W., 1982, A&A, 114, 245
van der Tak F. F. S., Schilke P., Müller H. S. P., Lis D. C., Phillips T. G., Gerin M., Roueff E., 2002, A&A, 388, L53
van Dishoeck E. F., Blake G. A., Jansen D. J., Groesbeck T. D., 1995, ApJ, 447, 760
Vassilev V. et al., 2008, A&A, 490, 1157
Walmsley C. M., Flower D. R., Pineau des Forêts G., 2004, A&A, 418, 1035

APPENDIX A: SPECTROSCOPIC DATA FOR NHD AND ND_2

Tables A1, A2, and A3, derived from the spectroscopic studies of Kobayashi et al. (1997), Motoki et al. (2013), Kanada et al. (1991), and Melosso et al. (2017), give the Einstein coefficients, transition frequencies, and quantum numbers relevant to this work. In the first three columns of each table, the first number is the upper level quantum number and the second one is the lower level quantum number.

Table A1. Frequencies and Einstein A_{ul} coefficients for the NHD ($N_{K_aK_c}J : 1_{01}\ 3/2–0_{00}\ 1/2$) hyperfine components.

F_1	F_2	F	Frequency (MHz)	A_{ul} (s^{-1})
1.5−1.5	2−1	3−2	412618.32	6.24×10^{-7}
1.5−1.5	2−1	2−1	412622.25	6.17×10^{-7}
1.5−1.5	2−1	1−0	412625.37	4.61×10^{-7}
1.5−1.5	2−1	1−1	412627.02	3.36×10^{-7}
0.5−1.5	0−1	1−0	412636.49	1.08×10^{-5}
0.5−1.5	0−1	1−1	412638.14	2.14×10^{-5}
0.5−1.5	0−1	1−2	412641.64	1.46×10^{-5}
1.5−1.5	1−1	2−1	412652.49	1.98×10^{-5}
0.5−1.5	1−2	2−2	412654.43	4.39×10^{-7}
1.5−1.5	1−1	2−2	412655.99	3.77×10^{-5}
0.5−1.5	1−2	1−1	412657.50	1.85×10^{-6}
1.5−1.5	1−1	1−0	412657.92	1.77×10^{-5}
1.5−1.5	1−1	1−1	412659.57	4.92×10^{-6}
1.5−1.5	1−1	0−1	412661.07	6.68×10^{-5}
0.5−1.5	1−2	0−1	412662.22	1.18×10^{-5}
0.5−1.5	1−2	2−3	412662.48	2.78×10^{-6}
0.5−1.5	1−2	1−2	412662.63	5.25×10^{-6}
1.5−1.5	1−1	1−2	412663.07	4.33×10^{-5}
1.5−1.5	2−2	3−2	412672.05	2.14×10^{-6}
1.5−1.5	2−2	2−1	412674.35	4.83×10^{-6}
1.5−1.5	2−2	1−1	412679.12	3.57×10^{-5}
1.5−1.5	2−2	2−2	412679.48	3.00×10^{-5}
1.5−1.5	2−2	3−3	412680.10	2.89×10^{-5}
1.5−1.5	2−2	1−2	412684.26	1.18×10^{-5}
2.5−1.5	2−1	3−2	412685.61	8.34×10^{-5}
1.5−1.5	2−2	2−3	412687.54	5.51×10^{-6}
0.5−0.5	1−1	2−1	412688.06	2.95×10^{-6}
2.5−1.5	2−1	2−1	412690.53	5.90×10^{-5}
0.5−0.5	1−1	2−2	412691.87	3.43×10^{-5}
2.5−1.5	2−1	1−0	412693.93	4.65×10^{-5}
2.5−1.5	2−1	2−2	412694.04	3.38×10^{-5}
2.5−1.5	2−1	1−1	412695.58	4.55×10^{-5}
0.5−0.5	1−1	1−1	412696.26	3.72×10^{-5}
0.5−0.5	1−1	1−0	412697.17	3.00×10^{-5}
2.5−1.5	2−1	1−2	412699.08	5.35×10^{-6}
0.5−0.5	1−1	1−2	412700.08	1.46×10^{-5}
0.5−0.5	1−1	0−1	412700.98	9.07×10^{-5}
0.5−0.5	1−0	2−1	412701.57	8.03×10^{-5}
1.5−1.5	1−2	2−1	412704.60	2.01×10^{-7}
2.5−1.5	3−2	4−3	412708.09	1.21×10^{-4}
2.5−1.5	3−2	3−2	412708.13	1.06×10^{-4}
2.5−1.5	3−2	2−1	412708.92	9.93×10^{-5}
1.5−0.5	2−1	3−2	412709.49	8.94×10^{-5}
1.5−1.5	1−2	2−2	412709.73	2.51×10^{-6}

Table A1 – *continued*

F_1	F_2	F	Frequency (MHz)	A_{ul} (s^{-1})
0.5−0.5	1−0	1−1	412709.77	3.17×10^{-5}
1.5−1.5	1−2	1−1	412711.67	4.04×10^{-6}
1.5−0.5	2−1	2−1	412713.11	5.92×10^{-5}
1.5−1.5	1−2	0−1	412713.17	1.35×10^{-5}
2.5−1.5	3−2	2−2	412714.05	2.08×10^{-5}
0.5−0.5	1−0	0−1	412714.49	1.80×10^{-5}
2.5−1.5	3−2	3−3	412716.18	1.48×10^{-5}
1.5−1.5	1−2	1−2	412716.80	1.02×10^{-5}
1.5−0.5	2−1	2−2	412716.93	1.90×10^{-5}
1.5−1.5	1−2	2−3	412717.78	1.36×10^{-5}
1.5−0.5	2−1	1−1	412717.88	3.11×10^{-5}
1.5−0.5	2−1	1−0	412718.80	3.85×10^{-5}
1.5−0.5	2−1	1−2	412721.70	2.17×10^{-6}
2.5−1.5	3−2	2−3	412722.10	6.49×10^{-7}
1.5−0.5	2−0	2−1	412726.62	1.82×10^{-6}
0.5−0.5	0−1	1−1	412729.00	1.88×10^{-5}
0.5−0.5	0−1	1−0	412729.91	9.56×10^{-6}
1.5−0.5	2−0	1−1	412731.40	9.01×10^{-7}
0.5−0.5	0−1	1−2	412732.81	3.30×10^{-5}
2.5−1.5	2−2	3−2	412739.34	5.26×10^{-6}
0.5−0.5	0−0	1−1	412742.51	1.29×10^{-5}
2.5−1.5	2−2	2−1	412742.64	4.44×10^{-6}
1.5−0.5	1−1	2−1	412743.36	1.11×10^{-5}
2.5−0.5	3−1	3−2	412745.57	3.26×10^{-7}
1.5−0.5	1−1	2−2	412747.17	2.05×10^{-5}
2.5−1.5	2−2	3−3	412747.39	2.61×10^{-5}
2.5−0.5	3−1	2−1	412747.68	2.06×10^{-7}
2.5−1.5	2−2	1−1	412747.68	1.18×10^{-5}
2.5−1.5	2−2	2−2	412747.77	1.18×10^{-5}
1.5−0.5	1−1	1−0	412751.34	2.39×10^{-6}
1.5−0.5	1−1	0−1	412751.93	4.06×10^{-6}
2.5−1.5	2−2	1−2	412752.81	6.06×10^{-6}
1.5−0.5	1−1	1−2	412754.25	1.45×10^{-5}
2.5−1.5	2−2	2−3	412755.82	5.98×10^{-6}
1.5−0.5	1−0	2−1	412756.87	1.57×10^{-5}
1.5−0.5	1−0	1−1	412763.95	2.40×10^{-5}
1.5−0.5	1−0	0−1	412765.45	3.68×10^{-5}
2.5−0.5	2−1	3−2	412776.78	6.23×10^{-6}
2.5−0.5	2−1	2−1	412781.40	2.96×10^{-6}
2.5−0.5	2−1	2−2	412785.21	2.78×10^{-6}
2.5−0.5	2−1	1−1	412786.44	2.67×10^{-6}
2.5−0.5	2−1	1−0	412787.35	2.44×10^{-6}
2.5−0.5	2−1	1−2	412790.25	4.40×10^{-7}
2.5−0.5	2−0	2−1	412794.91	3.60×10^{-7}

Table A2. Frequencies and Einstein A_{ul} coefficients for the NHD ($N_{K_aK_c}\,J:1_{01}\,1/2–0_{00}\,1/2$) hyperfine components.

F_1	F_2	F	Frequency (MHz)	A_{ul} (s^{-1})
1.5−1.5	1−1	0−1	413473.64	3.40×10^{-5}
1.5−1.5	1−1	1−0	413474.03	2.09×10^{-5}
1.5−1.5	2−1	1−0	413477.63	2.15×10^{-6}
1.5−1.5	1−1	1−2	413479.18	1.03×10^{-5}
1.5−1.5	2−1	1−1	413479.28	1.34×10^{-5}
1.5−1.5	2−1	2−1	413480.36	2.80×10^{-5}
1.5−1.5	2−1	1−2	413482.78	7.62×10^{-6}
1.5−1.5	1−1	2−1	413485.66	3.78×10^{-7}
1.5−1.5	1−1	2−2	413489.16	2.22×10^{-5}
1.5−1.5	2−1	3−2	413493.44	3.68×10^{-5}
1.5−1.5	1−2	0−1	413525.74	6.08×10^{-6}
1.5−1.5	1−2	1−1	413527.78	1.11×10^{-6}
1.5−1.5	2−2	1−1	413531.38	4.03×10^{-5}
1.5−1.5	2−2	2−1	413532.46	2.87×10^{-6}
1.5−1.5	1−2	1−2	413532.91	1.57×10^{-5}
1.5−1.5	2−2	1−2	413536.51	7.44×10^{-6}
1.5−1.5	2−2	2−2	413537.59	6.03×10^{-6}
1.5−1.5	1−2	2−1	413537.76	8.30×10^{-6}
0.5−1.5	1−1	1−0	413538.36	1.07×10^{-6}
0.5−1.5	1−1	2−1	413539.84	1.30×10^{-5}
0.5−1.5	1−1	1−1	413540.01	3.46×10^{-7}
0.5−1.5	1−1	0−1	413542.57	1.95×10^{-5}
1.5−1.5	1−2	2−2	413542.89	3.64×10^{-5}
0.5−1.5	1−1	2−2	413543.34	2.66×10^{-5}
0.5−1.5	1−1	1−2	413543.51	2.80×10^{-5}
0.5−1.5	0−1	1−0	413543.91	2.11×10^{-5}
0.5−1.5	0−1	1−1	413545.56	3.48×10^{-5}
1.5−1.5	2−2	2−3	413545.65	3.13×10^{-5}
1.5−1.5	2−2	3−2	413547.17	7.77×10^{-6}
0.5−1.5	0−1	1−2	413549.06	1.15×10^{-5}
1.5−1.5	1−2	2−3	413550.94	4.04×10^{-7}
1.5−1.5	2−2	3−3	413555.22	5.10×10^{-5}
1.5−0.5	1−1	0−1	413564.50	1.61×10^{-5}
1.5−0.5	1−1	1−1	413566.54	5.90×10^{-6}
1.5−0.5	1−1	1−0	413567.45	5.27×10^{-7}
1.5−0.5	2−1	1−1	413570.14	1.32×10^{-5}
1.5−0.5	1−1	1−2	413570.35	2.83×10^{-5}
1.5−0.5	2−1	1−0	413571.05	3.03×10^{-5}
1.5−0.5	2−1	1−2	413573.95	1.60×10^{-6}
1.5−0.5	2−1	2−2	413575.04	4.01×10^{-5}
1.5−0.5	1−1	2−1	413576.52	4.44×10^{-5}
1.5−0.5	1−0	0−1	413578.02	6.42×10^{-5}
1.5−0.5	1−0	1−1	413580.05	3.77×10^{-5}
1.5−0.5	1−1	2−2	413580.33	3.81×10^{-6}
1.5−0.5	2−0	1−1	413583.65	4.45×10^{-6}
1.5−0.5	2−1	3−2	413584.61	2.49×10^{-5}
1.5−0.5	2−0	2−1	413584.74	1.20×10^{-5}
1.5−0.5	1−0	2−1	413590.03	4.53×10^{-6}
0.5−1.5	1−2	2−1	413591.95	1.05×10^{-6}
0.5−1.5	1−2	1−1	413592.11	2.26×10^{-5}

Table A2 – *continued*

F_1	F_2	F	Frequency (MHz)	A_{ul} (s^{-1})
0.5−1.5	1−2	0−1	413594.68	8.92×10^{-5}
0.5−1.5	1−2	2−2	413597.08	1.28×10^{-5}
0.5−1.5	1−2	1−2	413597.24	5.58×10^{-5}
0.5−1.5	0−2	1−1	413597.66	3.38×10^{-6}
0.5−1.5	0−2	1−2	413602.79	8.33×10^{-6}
0.5−1.5	1−2	2−3	413605.13	6.04×10^{-5}
0.5−0.5	1−1	1−1	413630.87	5.55×10^{-6}
0.5−0.5	1−1	1−0	413631.78	5.20×10^{-6}
0.5−0.5	1−1	0−1	413633.43	1.01×10^{-5}
0.5−0.5	1−1	2−2	413634.52	3.32×10^{-7}
0.5−0.5	1−1	1−2	413634.68	1.56×10^{-6}
0.5−0.5	0−1	1−1	413636.42	6.42×10^{-6}
0.5−0.5	0−1	1−0	413637.33	1.93×10^{-6}
0.5−0.5	0−1	1−2	413640.24	2.46×10^{-5}
0.5−0.5	1−0	2−1	413644.22	6.26×10^{-6}
0.5−0.5	1−0	1−1	413644.38	3.55×10^{-7}
0.5−0.5	1−0	0−1	413646.95	1.66×10^{-6}
0.5−0.5	0−0	1−1	413649.94	8.48×10^{-6}

Table A3. Frequencies and Einstein A_{ul} coefficients for the para-ND_2 ($N_{K_aK_c}\,J:1_{11}\,1/2–0_{00}\,1/2$) hyperfine components.

F_1	F	Frequency (MHz)	A_{ul} (s^{-1})
1.5−1.5	0.5−0.5	530980.77	4.63×10^{-4}
1.5−1.5	1.5−0.5	530981.74	2.95×10^{-4}
1.5−1.5	0.5−1.5	530985.03	4.17×10^{-4}
1.5−1.5	1.5−1.5	530986.00	3.95×10^{-4}
1.5−1.5	2.5−1.5	530987.69	3.19×10^{-4}
1.5−1.5	1.5−2.5	530995.83	2.89×10^{-4}
1.5−1.5	2.5−2.5	530997.52	9.00×10^{-4}
1.5−0.5	0.5−1.5	531031.41	1.82×10^{-4}
1.5−0.5	1.5−1.5	531032.38	5.44×10^{-4}
1.5−0.5	2.5−1.5	531034.07	7.05×10^{-4}
1.5−0.5	0.5−0.5	531035.67	8.63×10^{-4}
1.5−0.5	1.5−0.5	531036.64	4.01×10^{-4}
0.5−1.5	1.5−0.5	531040.13	6.72×10^{-5}
0.5−1.5	0.5−0.5	531041.17	7.54×10^{-4}
0.5−1.5	1.5−1.5	531044.39	4.67×10^{-4}
0.5−1.5	0.5−1.5	531045.43	7.74×10^{-4}
0.5−1.5	1.5−2.5	531054.22	1.25×10^{-3}
0.5−0.5	1.5−1.5	531090.77	4.71×10^{-5}
0.5−0.5	0.5−1.5	531091.81	3.38×10^{-4}
0.5−0.5	1.5−0.5	531095.03	9.12×10^{-5}
0.5−0.5	0.5−0.5	531096.06	5.90×10^{-5}

This paper has been typeset from a TEX/LATEX file prepared by the author.